Heterogeneous Catalysis

DOI: 10.1002/anie.201104604

Dynamic X-Ray Diffraction Computed Tomography Reveals Real-Time Insight into Catalyst Active Phase Evolution**

Simon D. M. Jacques, Marco Di Michiel, Andrew M. Beale,* Taha Sochi, Matthew G. O'Brien, Leticia Espinosa-Alonso, Bert M. Weckhuysen, and Paul Barnes*

Dedicated to the Fritz Haber Institute, Berlin, on the occasion of its 100th anniversary

Metals and metal oxides anchored to porous support materials are widely used as heterogeneous catalysts in a number of important industrial chemical processes. These catalysts owe their activity to the formation of unique metal/metal oxide support interactions, typically resulting in highly dispersed 'actives' stabilized in a particular electronic or coordination state.[1–3] They are employed in fixed-bed reactors as extruded or pelletized millimeter-sized "catalyst bodies" minimizing pressure drops along the length of the reactor. Since the efficiency of the whole catalytic system depends on the behavior and efficiency of the catalyst body per se, its design has very great importance. Crucial to this design is an understanding of the factors which influence the distribution and nature of the active phase during preparation. The type of desired distribution is very much dependant on catalytic process and required products; for example, an egg-shell distribution (as opposed to uniform, egg-white, or egg-yolk), where the active phase is located at the edges of the catalyst body, can be favored if the product forms readily.[4,5]

Herein, we study catalyst bodies of nickel supported on γ-Al_2O_3. These catalysts are widely employed for hydrogenation.[1–3,6] They are often prepared using highly soluble nickel nitrate or chloride precursor salts, which allow for the preparation of catalysts with high metal loadings in a single impregnation step. Two problems are commonly encountered with the preparation of these catalysts: the formation of unwanted metal aluminate (spinel) phases and poor metal dispersion within the catalyst body. The dispersion of the metal ions within the alumina can be controlled by the addition of complexing agents to the impregnation solution, thereby changing the molecular structure of the precursor (through ligand exchange) as well as the interactions of the precursor with the support. Additionally, the presence of chelating ligands in the precursor increases both the metal oxide reducibility and dispersion.[7–10]

In recent times, absorption, spectroscopic, and scattering techniques have been developed to obtain spatial information on the distribution of chemical species in catalyst bodies, which allows the phenomena taking place during their preparation to be monitored.[7] These techniques include Raman, IR, and UV/Vis microspectroscopy; magnetic resonance imaging (MRI); tomographic energy dispersive diffraction imaging (TEDDI); and micro-computed tomography (μCT).[11–17] Importantly, both MRI and TEDDI are able to probe in a non-invasive manner in two dimensions, thus providing time-resolved information on both the impregnation and calcination/activation processes. Whilst the former is limited to the study of paramagnetic species and is therefore almost exclusively limited to probing the impregnation stage, TEDDI provides detailed information regarding elemental and crystalline phase distributions.[18,19] However, this technique currently suffers from a comparatively poor time resolution (on the order of hours) and instrument peak-width resolution. In this regard, a diffraction measurement technique that is capable of improving on the inherent weaknesses of TEDDI would represent a significant advancement. Herein, we describe dynamic X-ray diffraction computed tomography (XRD-CT) and demonstrate its capability to image a catalyst body impregnated with a Ni-(en)-Cl precursor (en = ethylenediamine) undergoing a thermal treatment as a route to the formation of the active phase. XRD-CT[20–26] requires that the sample is exposed to X-ray radiation with a series of transmission "projection" measurements being made at several angles. An image slice is then reconstructed from these measurements using a suitable algorithm. This approach is currently utilized for recording computerized tomography (CT) images, although instead of using a contrast image based on the differences in absorption of the irradiating radiation along the different projections, XRD-CT makes use of differences in the diffraction signals for the crystalline phases present. It follows that, in a manner akin to CT, the concentration of individual solid-state chemical species can be mapped within an object (by for

[*] Dr. S. D. M. Jacques, Dr. A. M. Beale, Dr. M. G. O'Brien, Dr. L. Espinosa-Alonso, Prof. Dr. B. M. Weckhuysen
Inorganic Chemistry and Catalysis
Debye Institute for Nanomaterials Science, Utrecht University
Universiteitsweg 99, 3584 CG Utrecht (The Netherlands)
E-mail: s.d.m.jacques@uu.nl
a.m.beale@uu.nl

Dr. S. D. M. Jacques, T. Sochi, Prof. Dr. P. Barnes
Department of Chemistry, University College London
20 Gordon Street, London WC1H 0AJ (UK)
and
Department of Crystallography, Birkbeck College
Malet Street, London WC1E 7HX (UK)

Dr. M. Di Michiel
ESRF, 6 Rue Jules Horowitz, 38000 Grenoble (France)

[**] We kindly acknowledge funding from the EPSRC (UK) and ACTS-ASPECT (The Netherlands) as well as beam time from the ESRF. We also wish to express their gratitude to Dr. M. Peel for his help with the initial experimental setup.

Supporting information for this article is available on the WWW under http://dx.doi.org/10.1002/anie.201104604.

example, taking a representative peak for that phase), and, indeed any additional information available within the diffraction signal can be used. To achieve dynamic scans on these objects with reasonable time resolution requires a high flux, high-energy X-ray source, and suitably fast detection, all of which are available at modern synchrotron radiation facilities.[22,27,28]

We present the results of a dynamic 2D XRD-CT in situ study showing 22 time slices (Figure 1 and Figure 2a) recorded at one vertical position in the sample as well as 3D XRD-CT results obtained before and after the in situ experiment (Figure 3) covering the entire sample.

Figure 1 shows a stack plot of the sum of diffraction patterns for each slice. Nine separate crystalline phases are identifiable from these data which were either identified by comparison with reference patterns from the ICSD or else, where no reference patterns exist (i.e., for the (en)-containing phases), phase assignment is proposed based on both previous literature and comparative analysis of temperature-programmed MS desorption data (ESI).[29] Initially, from a diffraction perspective only peaks corresponding to reflections for the γ-Al_2O_3 support phase were observed at room temperature. No crystalline Ni-containing phases were observed, although UV/Vis spectroscopy reveals that Ni is present on the support as the complex $Ni(en)(H_2O)_2(Al{-}O)_2$.[15] As the temperature approaches 100 °C, the complex reacts with the dissociated Cl^- species and CO_2 to form $Ni(en)(CO_3)_xCl_{2(1-x)}{\cdot}x\,H_2O$ characterized by a broad peak at 0.9° 2θ. As the temperature rises to first 325, then 400, 450, and eventually 500 °C, this crystalline phase undergoes subsequent dehydration and decomposition, resulting in the formation of a number of intermediate phases including first

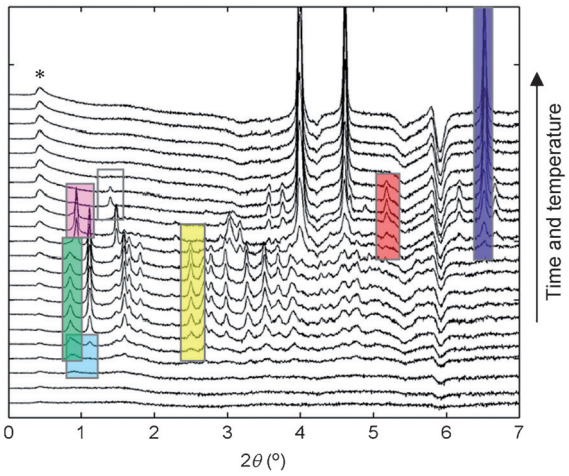

Figure 1. Stack plot of summed diffraction patterns recorded in each temporal slice. For each recorded time slice, the diffraction from the 1290 recorded projections has been summed. The sum of diffraction for the first slice is subtracted and a fixed offset is added for display purposes. In this way we can see the evolving diffraction as the experiment proceeds. The colored boxes indicate features of interest which have been extracted, and it is these features that have been reconstructed spatially in Figure 2 and the Supporting Information (with the corresponding color scheme). The (*) denotes an unidentified contribution to the data.

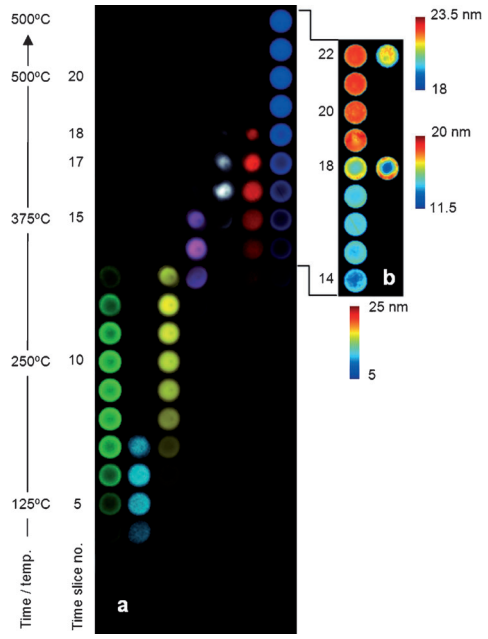

Figure 2. Reconstructed 2D images of features observed in the diffraction patterns as a function of time and temperature during thermal activation of a γ-Al_2O_3-supported Ni catalyst precursor. a) The color maps indicate the following distribution of solid-state phases accordingly: $Ni(en)_xCO_3$ (green), $Ni(en)(CO_3)_xCl_{2(1-x)}{\cdot}x\,H_2O$ (cyan), $Ni(en)(CO_3)_xCl_{2(1-x)}$ (yellow), $Ni(en)_{0.5}(O)_xCl_{2(1-x)}$ (magneta), $Ni(en)Cl_2$ (white), hcp Ni (red), and fcc Ni (blue) b) The thermal color maps show the variation in crystallite size (nm). When plotted with a common color axis (below), these indicate the growth of fcc Ni crystallite size as the growth of the phase proceeds. For time slices 18 and 22, the data have been re-plotted with bespoke color axes (right).

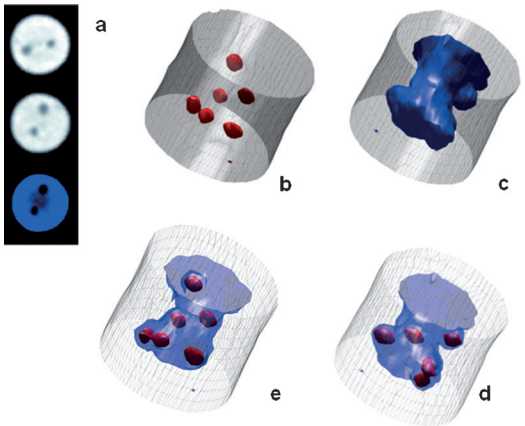

Figure 3. 3D XRD-CT images of a catalyst body. a) Selected 2D slices of the alumina distribution before (top) and after (middle) calcination, and the fcc Ni phase distribution (bottom) after calcination. The apparent change in the voids' positions is due to sample movement during calcination. b–e) Isosurface maps of sample features as measured before (b) and after (c–e) calcination generated by mapping a surface which encloses all voxels below a certain intensity; In each, the uncapped wire mesh (gray) corresponds to the physical boundaries of the catalyst body. b) The red isosurfaces bound 0% alumina intensity (showing the voids) and c) blue isosurfaces enclose voxels below 33% of the maximum recorded intensity for fcc Ni. d) A reproduction of (c), but the blue isosurface has been made partially transparent. e) A rotated version of (d) for comparison to (b) that is corrected for sample movement.

$Ni(en)(CO_3)_xCl_{2(1-x)}$ (strong peaks at 1.11, 1.58, 1.65, 2.48, 2.68, 2.77, 2.96, 3.26, and 3.50° 2θ), $Ni(en)_{0.5}(O)_xCl_{2(1-x)}$ (strong peaks at 0.93 and 1.47° 2θ)), and $Ni(en)Cl_2$ (strong peak at 1.39° 2θ), hexagonal close-packed (hcp) Ni (strong peaks at 3.57, 3.76, 4.07, 5.18, and 6.16° 2θ) and finally face-centered cubic (fcc) Ni (strong peaks at 3.99, 4.61, 6.53° 2θ) respectively. Previously, due to a combination of a lack of sufficient data quality and kinetic resolution, it was not possible to 1) determine the nature of the first Ni-containing crystalline phase, 2) observe in such detail this stepwise decomposition leading to the formation of a number of intermediate species, and finally 3) to differentiate the presence of hcp Ni from Ni_3C.[16,30] Distinguishing between Ni_3C and hcp Ni is now possible from the data since reliable peak intensities can be extracted; the relative intensity of the reflection at 6.16° 2θ is more consistent with the presence of hcp Ni than Ni_3C.

The data presented in Figure 1 are akin to the 'traditional' in situ time-resolved result, although these data are more representative since they represent an entire 2D section. These data can also be reconstructed to produce phase distribution maps, and these are shown in Figure 2a. These have been produced by using at least one unique "diagnostic" diffraction peak for each phase, but could be equally produced by using a Rietveld phase scale factor.[22] The color maps show the distribution of the phases shown in the 1D stack plot and reveal that the solid-state evolution process exhibits spatial variation. By doing this, we were also able to identify the presence of an additional initial phase ($Ni(en)_xCO_3$).

The time-resolved 2D data clearly reveal that the phase evolution as seen in the 1D data is non-uniform and that there are two decomposition pathways leading to the appearance of the fcc Ni phase after calcination. These two pathways are dictated by the two crystalline phases that form at the beginning of calcination around 100–125 °C. The phases comprise an $Ni(en)_xCO_3$ phase (green) at the periphery (egg-shell) and $Ni(en)(CO_3)_xCl_{2(1-x)}\cdot x\,H_2O$ phase (cyan), which possesses an egg-white distribution. The former ($Ni(en)_xCO_3$ phase) decomposes at approximately 325 °C, leading to the first appearance of the fcc Ni phase possessing the same egg-shell distribution. The $Ni(en)(CO_3)_xCl_{2(1-x)}\cdot y\,H_2O$ phase on the inside of the pellet undergoes dehydration at approximately 175 °C yielding $Ni(en)(CO_3)_xCl_{2(1-x)}$, with subsequent CO_2/en loss at approximately 300 °C to form $Ni(en)_{0.5}(O)_xCl_{2(1-x)}$ and "O" and en loss from approximately 325 °C by a disproportionation reaction to yield $Ni(en)Cl_2$ and hcp Ni. Above 400 °C, $Ni(en)Cl_2$ and hcp Ni phase disappear to yield fcc Ni, so that on reaching 500 °C this is distributed across the entire sample.

In addition to the crystalline phases, a 300 μm diameter dark circle (with zero scattering intensity) can be seen, suggestive of voids being initially present within the pellet (several such voids are seen in the 3D maps, see below). The void remains stable during calcination and is impervious to either the Ni precursor or the subsequently formed crystalline species. It should be noted that there is sample movement between the 17th and 18th time slice (this is confirmed from before and after 3D scans) and is not an artifact of reconstruction. The presence of such voids has been independently confirmed by standard microtomography (see Figure S9 in the Supporting Information).

The data recorded from these measurements are of sufficient quality that it is possible to extract additional structural information. In Figure 2b, we show the fcc Ni crystallite size as derived from the Scherrer analysis of the full width at half maxima (FWHM) of the (220) fcc Ni reflection. The maps at the top of Figure 2b show the crystallite size with a common color axis to indicate the size distribution within the pellet and the subsequent crystallite growth as a function of temperature/time. For slices 18 and 22, the data have been re-plotted with bespoke color axes. At slice 18, smaller crystallites of fcc Ni are found in the center (larger crystallites are seen at the cylinder periphery), reflecting the lag in phase growth in this region. At slice 22, whilst the pellet contains a uniform phase distribution, the crystallite size distribution is uneven; larger crystallites are observed on the inside (egg-white) rather than towards the rim. The larger particles form where appreciable amounts of $Ni(en)Cl_2$ were previously observed, which is therefore suggestive of the effect of chlorine promoting particle sintering and growth.[31] $Ni(en)Cl_2$ is not seen at the periphery since the initial crystalline phase that appears ($Ni(en)_xCO_3$) does not contain Cl.

Figure 3 shows the γ-Al_2O_3 distribution as measured before calcination and the γ-Al_2O_3 and fcc Ni distributions after in situ calcination. Figure 3a contains a comparison from the 2D projections whereas Figures 3b–d) contain 3D images constructed from a series of projections taken in 300 μm steps down the length of the pellet. In Figure 3b the wire-net isosurface (gray) encloses all voxels below the maximum recorded alumina intensity and results in a cylinder corresponding to the physical boundaries of the catalyst body. This wire-net cylinder is transparent and un-capped at each end in order that the isosurface corresponding to the voids (red) are visible. These voids can be thought of as a 'negative' image created, by enclosing all voxels within the body which have 0% alumina intensity. Confirmation of the voids can be seen in the μCT data shown in Figure S9. In Figure 3c and d the wire-net cylinders have been created by an isosurface bounding the maximum recorded fcc Ni intensity. The blue isosurfaces then enclose all voxels below 33% of the maximum recorded intensity for this phase. In Figure 3d the latter has been made partially transparent, to reveal the voids. The voids in Figure 3d appear in physically different positions to those in Figure 3b due to sample movement (see above), however this discrepancy can be corrected by rotation of the cylinder by 130° and a small shift in z; the rotated version for comparison to Figure 3b is shown in Figure 3e. Clearly evident from the images of both the precalcination and postcalcination data Figure 3b,d are a plethora of voids distributed along the length of the sample, revealing a large "dead volume" unavailable as a catalyst support. The voids remain stable during calcination, with fcc Ni forming around them. The fcc Ni distribution itself possesses a dumbbell-shaped distribution; the negative map shows that more fcc Ni has grown around the midrift of the body than has grown near the top or bottom. The cause of this uneven growth is not fully understood, but in all likelihood it is related to the presence

and distribution of $Ni(en)Cl_2$; a temporal study, but with the body aligned with its longitudinal axis perpendicular to the CT rotation axis, would be able to confirm this hypothesis.

The obtained images constitute a totally new way of monitoring intricate chemistry in space and time within materials. The results presented clearly show that the formation of the final catalyst active phase is a complex, multistep process and that the catalyst body possesses both an inhomogeneous structure and phase composition in both 2D and 3D. Such observations could have important implications for the preparation and subsequent catalytic activity of such samples and will thus be of particular interest to the heterogeneous catalysis community. The developed technique has had and should have future impact upon a range of disciplines and materials, for example, phase transformations and dynamic stress imaging of construction or biological materials such as concrete, alloys, bone.[21,25] Furthermore, the continued advancements in X-ray generation and collection technology promise even higher time and spatial resolution for such studies in the not too distant future.

Experimental Section

The experiments were performed at station ID15B of the ESRF (Grenoble, France) using a monochromatic $E = 86.88$ keV 100 μm square section pencil beam with diffracted X-rays recorded on a Pixium 4700 flat panel detector. Dynamic diffraction imaging was employed to monitor the in situ calcination (ambient to 500 °C at 2.5 °C min^{-1} with dwell of 2 h) of a cylindrical catalyst body (diameter = 3 mm; length = 3 mm) impregnated with a Ni catalyst precursor material ($[NiCl_2(en)(H_2O)_4]$ where en = ethylenediamine). The calcination was performed under flowing He; this necessitated mounting the catalyst body within a gas-tight environment which consisted of a quartz cell and gas delivery stub. The latter was fixed to a goniometer attached to a rotation stage. This entire setup itself was mounted upon a translation stage, onto which were also mounted two heat guns; this setup allowed for the translation of the heating guns with the sample. Annotated photographs of the experimental setup are shown in Figure S1 for comparison to the schematic inset in Figure S2 in the Supporting Information.

For each time slice, diffraction was recorded at 43 translations spaced 100 μm across the body each with 30 rotations of 6°, corresponding to 1290 projections. Each diffraction pattern was recorded for 400 ms. Accounting for dead time and stage movement, time each slice was acquired in approximately 600 s. The samples yielded powder ring data, and these were radially integrated for each diffraction "projection". For each observed intensity in these radially integrated patterns (i.e. for all 2θ values), a sinogram was constructed and then back-projected to a 43×43 pixel image. For N values of 2θ, this yielded N real-space reconstructed images. It follows that any vector perpendicular to such a stack of images will yield a reconstructed diffraction pattern corresponding to the selected volume element in the slice (this approach and an alternative are outlined in Figure S2 in the Supporting Information). Features extracted (by pattern decomposition) from these reconstructed diffraction patterns are presented herein, that is, for both the time-resolved data (performed at the middle in terms of length of the catalyst body) and the 3D static images (a series of 10 2D slices were measured along the length of the catalyst body before and after the calcinations step). The processing and analysis of the considerable volume of diffraction data collected (over 50000 diffraction patterns) required the development of dedicated high-throughput software.[32]

Received: July 4, 2011
Published online: September 20, 2011

Keywords: catalyst preparation · chemical imaging · computed tomography · heterogeneous catalysis · X-ray diffraction

[1] *Preparation of Solid Catalysts* (Eds.: G. Ertl, H. Knozinger, J. Weitkamp), Wiley-VCH, Weinheim, **1999**.
[2] *Catalyst Preperation: Science and Engineering* (Ed.: J. Regalbuto), CRC, Boca Raton, **2007**.
[3] *Synthesis of Solid Catalysts* (Ed.: K. P. De Jong), Wiley-VCH, Weinheim, **2009**.
[4] A. V. Neimark, L. I. Kheifez, V. B. Fenelonov, *Ind. Eng. Chem. Prod. Res. Dev.* **1981**, *20*, 439.
[5] K. Bourikas, C. Kordulis, A. Lycourghiotis, *Catal. Rev. Sci. Eng.* **2006**, *48*, 363.
[6] R. Struis, T. J. Schildhauer, I. Czekaj, M. Janousch, S. M. A. Biollaz, C. Ludwig, *Appl. Catal. A* **2009**, *362*, 121.
[7] L. Espinosa-Alonso, A. M. Beale, B. M. Weckhuysen, *Acc. Chem. Res.* **2010**, *43*, 1279.
[8] E. Marceau, A. Lofberg, J. M. Giraudon, F. Negrier, M. Che, L. Leclercq, *Appl. Catal. A* **2009**, *362*, 34.
[9] F. Négrier, E. Marceau, M. Che, J. M. Giraudon, L. Gengembre, A. Lofberg, *Catal. Lett.* **2008**, *124*, 18.
[10] F. Négrier, E. Marceau, M. Che, J. M. Giraudon, L. Gengembre, A. Lofberg, *J. Phys. Chem. B* **2005**, *109*, 2836.
[11] J. A. Bergwerff, T. Visser, B. R. G. Leliveld, B. D. Rossenaar, K. P. de Jong, B. M. Weckhuysen, *J. Am. Chem. Soc.* **2004**, *126*, 14548.
[12] A. A. Lysova, I. V. Koptyug, R. Z. Sagdeev, V. N. Parmon, J. A. Bergwerff, B. M. Weckhuysen, *J. Am. Chem. Soc.* **2005**, *127*, 11916.
[13] L. G. van de Water, J. A. Bergwerff, T. A. Nijhuis, K. P. de Jong, B. M. Weckhuysen, *J. Am. Chem. Soc.* **2005**, *127*, 5024.
[14] A. M. Beale, S. D. M. Jacques, J. A. Bergwerff, P. Barnes, B. M. Weckhuysen, *Angew. Chem.* **2007**, *119*, 8988; *Angew. Chem. Int. Ed.* **2007**, *46*, 8832.
[15] L. Espinosa-Alonso, K. P. de Jong, B. M. Weckhuysen, *J. Phys. Chem. C* **2008**, *112*, 7201.
[16] L. Espinosa-Alonso, M. G. O'Brien, S. D. M. Jacques, A. M. Beale, K. P. de Jong, P. Barnes, B. M. Weckhuysen, *J. Am. Chem. Soc.* **2009**, *131*, 16932.
[17] J. D. Grunwaldt, B. Kimmerle, A. Baiker, P. Boye, C. G. Schroer, P. Glatzel, C. N. Borca, F. Beckmann, *Catal. Today* **2009**, *145*, 267.
[18] C. Hall, P. Barnes, J. K. Cockcroft, S. D. M. Jacques, A. C. Jupe, X. Turrillas, M. Hanfland, D. Hausermann, *Anal. Commun.* **1996**, *33*, 245.
[19] R. J. Cernik, K. H. Khor, C. Hansson, *J. R. Soc. Interface* **2008**, *5*, 477.
[20] G. Harding, J. Kosanetzky, U. Neitzel, *Med. Phys.* **1987**, *14*, 515.
[21] G. Harding, J. Kosanetzky, *Nucl. Instrum. Methods Phys. Res. Sect. A* **1989**, *280*, 517.
[22] P. Bleuet, E. Welcomme, E. Dooryhee, J. Susini, J. L. Hodeau, P. Walter, *Nat. Mater.* **2008**, *7*, 468.
[23] L. Valentini, M. C. Dalconi, M. Parisatto, G. Cruciani, G. Artioli, *J. Appl. Crystallogr.* **2011**, *44*, 272.
[24] M. Álvarez-Murga, P. Bleuet, L. Marques, C. Lepoittevin, N. Boudet, G. Gabarino, M. Mezouar, J. L. Hodeau, *J. Appl. Crystallogr.* **2011**, *44*, 163.

[25] G. Artioli, T. Cerulli, G. Cruciani, M. C. Dalconi, G. Ferrari, M. Parisatto, A. Rack, R. Tucoulou, *Anal. Bioanal. Chem.* **2011**, *397*, 2131.
[26] F. Basile, P. Benito, S. Bugani, W. De Nolf, G. Fornasari, K. Janssens, L. Morselli, E. Scavetta, D. Tonelli, A. Vaccari, *Adv. Funct. Mater.* **2010**, *20*, 4117.
[27] A. M. Beale, S. D. M. Jacques, B. M. Weckhuysen, *Chem. Soc. Rev.* **2010**, *39*, 4656.
[28] M. G. O'Brien, A. M. Beale, S. D. M. Jacques, M. Di Michiel, B. M. Weckhuysen, *Appl. Catal. A* **2011**, 391, 468.
[29] S. Dash, P. K. Ajikumar, M. Kamruddin, A. K. Tyagi, *Thermochim. Acta* **1999**, *334*, 141.
[30] V. Rodríguez-González, E. Marceau, P. Beaunier, M. Che, C. Train, *J. Solid State Chem.* **2007**, *180*, 22.
[31] Y. H. Choi, W. Y. Lee, *Catal. Lett.* **2000**, *67*, 155.
[32] T. Sochi, S. D. M. Jacques, P. Barnes, **2010**, EasyDD software. Available on request by e-mailing r5896329@yahoo.co.uk.

